ELSEVIER

International Journal of Solids and Structures 41 (2004) 3439–3459

INTERNATIONAL JOURNAL OF SOLIDS and STRUCTURES

www.elsevier.com/locate/ijsolstr

Characterisation of materials subjected to large strains by inverse modelling based on in-plane displacement fields

J. Kajberg *, G. Lindkvist

Division of Solid Mechanics, Luleå University of Technology, SE-97187 Luleå, Sweden

Received 4 November 2003; received in revised form 9 February 2004
Available online 27 March 2004

Abstract

A method for characterisation of materials subjected to large strains beyond the levels when plastic instability occurs in standard tension tests is presented. Thin sheets of two types of hot-rolled steel are subjected to tension loading until fracture occurs. The deformation process is captured with a digital camera and by digital speckle photography (DSP) in-plane pointwise displacement fields are obtained. By numerical differentiation and assuming plastic incompressibility the equivalent plastic strain is determined. The characterisation performed in this paper consists of estimating material parameters in two constitutive models. These models are a piecewise linear plasticity model and a parabolic hardening model. By using inverse modelling including finite element analyses (FEA) of the tension tests the material parameters are adjusted to achieve a minimum in a so-called objective function. The objective function is basically a least-square functional based on the difference between the experimental and FE-calculated displacement and strain fields. Due to the large deformations an adaptive meshing technique is used in order to avoid highly distorted elements. The DSP-technique provided measurements, where the uncertainty of the equivalent plastic strain varied between 0.0015 and 0.0056. The maximum obtained strain was approximately 0.8. The true stress–strain curves based on the estimated parameters are validated in the low strain region by comparison with curves from standard tension tests.

Keywords: Constitutive behaviour; Inverse modelling; Strain localisation; Digital speckle photography (DSP)

1. Introduction

Increased access to powerful computers at relatively low costs has made the use of computer aided engineering (CAE) systems almost mandatory in the manufacturing industry. The finite element method (FEM) is considered to be the most powerful tool within the CAE systems because it can handle large degree of freedom simulations with a wide range of working conditions (Mori et al., 1995). FEM is a widely used numerical simulation instrument in the field of metal forming processes.

The development of a new product in the metal forming industry is a process involving several steps. Generally it involves design and manufacturing of a number of prototypes, both of the detail intended for

* Corresponding author. Tel.: +46-920-491045; fax: +46-920-491047.
E-mail address: Jorgen.Kajberg@ltu.se (J. Kajberg).

0020-7683/$ - see front matter © 2004 Elsevier Ltd. All rights reserved.
doi:10.1016/j.ijsolstr.2004.02.021

production and of the forming tool to be used. The use of predictive engineering, or simulation, is a way of reducing the number of prototypes needed and the time used for testing of the product when going from concept to production. This is especially important for the prototyping of the tool, because it is generally very expensive to manufacture several prototypes or to refine one already built (Adams and Askenazi, 1999).

Simulation of a metal forming process is a complex problem because the physical process involves highly non-linear parts such as large material deformation, history dependent material behaviour and complex contact phenomena. Recalling that a finite element analysis (FEA) is the solution of a mathematical model of a structural behaviour, the implication must be that the solution is never more accurate than the model permits. Using non-linear constitutive equations in a simulation causes some difficulties. First of all, most non-linear equations describing material behaviour, although varying in complexity, are to some extent very simplified approximations (e.g. elastic–plastic models used for modelling of metals during complex stress paths). Also, elastic–plastic models are often used beyond the range of available data (Belytschko and Mish, 2001). Still, even if a very complex model is used, the problem of determining the appropriate model parameters exists and in order to get reliable results from a metal forming simulation, one important prerequisite is that the material model is accurate. Here this means that the parameters in the chosen constitutive model are estimated in the best possible way.

The most common way to evaluate the stress–strain relationship for a material is by performing standardised tension tests (ASTM Standard E8M-96, 1996). These tests require specimens subjected to a homogeneous state of uniaxial loading. Typically, the specimens are long round bars or thin sheets with rectangular cross-section subjected to tension loading in a common tension testing machine. According to the standard mentioned above uniaxial strain is determined by using a so-called extensometer that measures the extension of a certain gauge length. The relative extension, i.e. the fraction between the measured extension and the gauge length, then gives a value of the uniaxial (engineering) strain. The shortcoming of this testing procedure is that the assumption of uniformity is valid only until the maximum load is achieved. Thereafter plastic instability and strain localisation will occur and the so-called diffuse necking starts. This phenomenon might cause the specimen to terminate in fracture, but for thin sheet it is often followed by a second instability process, namely localised necking. The difference between these two types of necking is shown in Fig. 1, where the onset of diffuse necking occurs as a decrease of the width of the specimen. When the later upcoming localised neck appears the width of the specimen decrease only slightly, but the thickness along the necking band shrinks rapidly and soon thereafter fracture occurs.

If the strain is determined by using an extensometer according to ASTM Standard E8M-96 (1996), the resulting value beyond the onset of necking will be an underestimation of the actual strain. Also, in pressworking operations the strain can locally reach magnitudes significantly higher than what is possible to obtain from a standard tensile test. Several methods (Bridgman, 1952; Ling, 1996; Zhang et al., 1999, 2001) are developed to correct and compensate for the necking occurrence in order to extend the region of validity for the standard testing procedure.

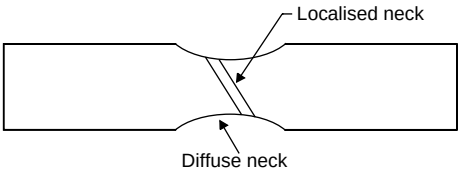

Fig. 1. Different types of necking.

Another possibility to extend the range of application for a material model is proposed by Ghouati and Gelin (1998, 2001), where the FEM is combined with an optimisation algorithm. The general idea in the papers is to use the forming operation which the material is subjected to in the parameter estimation process. Adjustments of the material parameters in the simulation are made in order to get the calculated response from the FEA to match the measured response (in a least-square sense) from the forming operation. However, this methodology is not applicable when a prototype of a forming tool is unavailable, i.e. there is no physical large-scale or production forming process present for comparison.

The purpose of this paper is to suggest a method for determination of the stress–strain relationship that is valid for strains above the levels restricted by the necking phenomenon in the standard testing procedure. The method presented here is based on inverse modelling (Tarantola, 1987).

The basic approach in inverse modelling is to employ a so-called objective function that measures the agreement between some experimental data and a numerical model, i.e. a finite element simulation. The model describes the experimental response and is supplied with a particular choice of material parameters in a constitutive model. The parameters are then adjusted to achieve a minimum in the objective function, yielding best-fit parameters. The adjustment process is thus a problem of optimisation in many dimensions. Using this method will in most cases provide a set of optimal parameters. The application of inverse modelling is presented in, for example, Mahnken and Stein (1994), Faurholdt (2000) and Kajberg et al. (2004).

In this paper, the experimental data is provided by tension tests of thin sheet specimens. The state of deformation is quantified by an optical method, digital speckle photography (DSP), providing field information for both in-plane displacements and strains. The demand of uniformity no longer has to be fulfilled and furthermore, no correction method to compensate for the multiaxial stress–strain state in the necking region is necessary.

In this work, the chosen constitutive models are: a piecewise linear plasticity model, and a parabolic hardening model. Both models are employed in an implicit finite element (FE) code, MSC.Marc (2003).

2. Experiments

2.1. Specimen design

The DSP-method, which so far is designed to measure in-plane displacements implies that it is most suitable for measurement on thin sheets, where the dominating displacement components are the in-plane ones. The DSP-method is here used to capture the dramatically deforming region, where the necking occurs, for thin sheet specimens. However, for specimens with uniform cross-section it is difficult to predict where along the specimens the plastic instability starts and in order to achieve a good spatial resolution the camera should be focused on the necking region. The specimens (Fig. 2) are therefore machined with a narrow part in the middle, where the plastic deformations and the upcoming plastic instability are forced to appear. The captured narrow region of a specimen is depicted as a shaded square in Fig. 2.

The materials, which are chosen in the investigation, are two hot-rolled steels, Domex 355 and Domex 650, with yield stresses of at least 355 and 650 MPa, respectively. The tests are performed in a common tension testing machine, where the specimens are subjected to controlled displacements at rates of 0.025 and 0.0125 mm/s for Domex 355 and Domex 650, respectively. The time to complete a tension test, i.e. to load the specimen until fracture, varied between 70 and 110 s. The longer times were required for the specimens made of Domex 650. The loading forces are measured by the tension testing machine for further use in the parameter estimation.

In order to validate the estimated material parameters standard tension tests (ASTM Standard E8M-96, 1996) are performed. Here, the specimens consist of thin sheets with thickness of 1 mm, width of 6 mm and

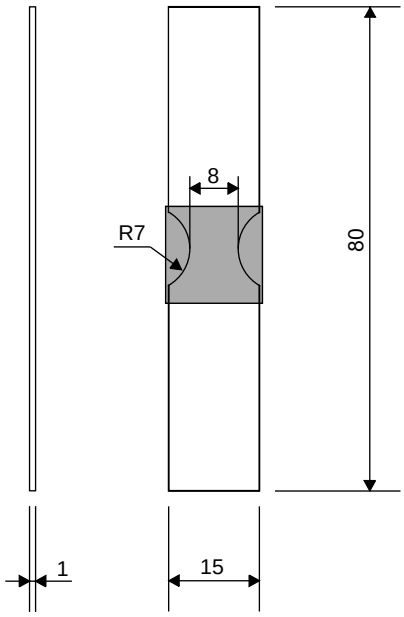

Fig. 2. Specimen design. All numbers are in [mm].

a gauge length (part of the specimen with constant cross-section) of 32 mm. Four specimens of each material, Domex 355 and Domex 650, are used in the standard tests.

2.2. Displacement and strain measurement through speckle photography

By using DSP it is possible to detect the complete in-plane displacement field of a specimen. Further, the strain field can be evaluated by numerical differentiation of the displacement field data.

The most fundamental requirement for the DSP-method, that there exists a random pattern at the object surface, is accomplished by using diffusely reflecting black and white spray paint. The randomness ensures that any small region of the object surface is unique. By capturing the object surface with a digital camera before and after the object has been subjected to some kind of displacement or deformation any small unique region can be tracked by using a cross-correlation procedure (Sjödahl, 1994). In order to get field data the object surface is divided into a large number of small regions, so-called subimages. In this case the entire image of the object surface consists of 512×512 pixels and the chosen sizes of the subimages are 16×16 or 32×32 pixels depending on their positions. The relative positions of their midpoints are depicted in Fig. 3(a), which represents the initial grid configuration of subimages. The midpoints are separated by approximately half the size of the subimages they are representing. The separation defines the spatial resolution of the evaluated displacement field. Note that the subimages are placed tighter in the middle of the specimen, where the neck, i.e. plastic instability is assumed to occur.

The cross-correlation procedure does not take into account any deformation or rotation of the subimages. This means that the subimages are not reshaped in order to take care of any strains or rotations in the small regions they cover. In this specific case, when large deformations (i.e. high strain values) take place, a new grid configuration is created by updating the positions of the subimages in the initial grid configuration. The subimages are thereby given new positions for the next correlation by compensating for their evaluated displacements. However, the speckle displacements and thereby the new coordinates for the

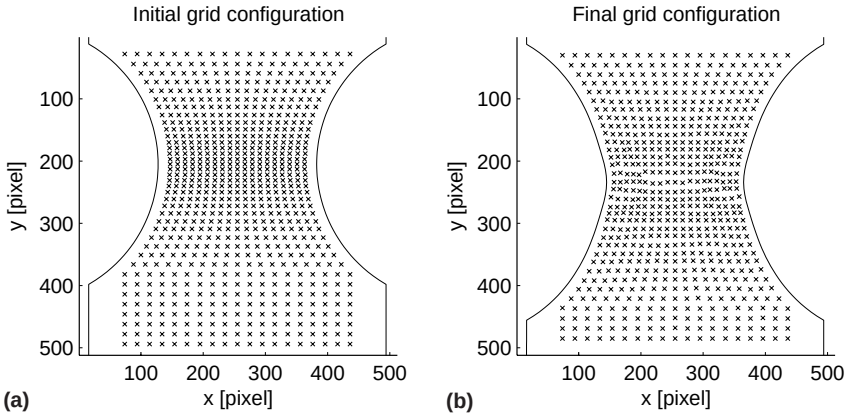

Fig. 3. Initial positions of the subimages (a). Final positions of the subimages (b). The crosses indicate the midpoints of the subimages.

updated grid are not integer numbers, which is necessary in the correlation procedure. Therefore, the nearest pixel locations are chosen as basis for the next displacement evaluation. The introduced errors by using the nearest pixel as basis are assumed to be negligibly small since the displacement field is smooth.

Up to 15 grid updates are used in the presented tests. The final grid configuration is shown in Fig. 3(b). During the tension tests two pictures are taken every second. However, not all of the images are used in the evaluation. Instead an iterative search algorithm is used to find the image resulting in an increment of 5% of the maximum detected equivalent plastic strain. Therefore, field information regarding displacements and strains is evaluated at equispaced strain increments instead of fixed time intervals. Two features can be noted. Firstly, the field information is uniformly spread across the interval of the measured strains. If field data instead is evaluated at fixed time intervals the strain with lower values would dominate in the subsequent inverse modelling since the strain values increase more rapidly towards the end of the test compared to the beginning. Secondly, every speckle displacement contains small random errors, which are added for every evaluation step. The errors are discussed later. The choice of an increment of 5% is thus a compromise between the decorrelation, which appear when the subimages become strained or rotated, and the additive error corresponding to the displacement increments.

The displacement field contains all the information needed to calculate the in-plane strain and shear components ε_x, ε_y and ε_{xy}. By assuming plastic incompressibility also the out-of-plane (normal) strain component ε_z is possible to deduce. The evaluation of the strain matrix is first described for a general case.

Due to the large displacements the true (logarithmic) strain definition is chosen for representation of the strain state. In order to derive the true strain components the so-called deformation gradient matrix $\mathbf{F}$ has to be considered. This matrix describes the relative spatial position of two neighbouring particles after deformation in terms of their relative material position before deformation. The matrix takes the form

$$\mathbf{F} = \frac{\partial \mathbf{x}'}{\partial \mathbf{x}} \tag{1}$$

where $\mathbf{x}$ refers to the initial (material) Cartesian coordinates and $\mathbf{x}'$ describes the current (spatial) Cartesian coordinates. Most of its components are directly determined by considering the experimental displacement information.

In order to derive the true strain, $\mathbf{F}$ is decomposed into a rotation matrix $\mathbf{R}$ and a stretch matrix $\mathbf{V}$ (Bonet and Wood, 1997) according to

$$\mathbf{F} = \mathbf{V} \cdot \mathbf{R} \tag{2}$$

The stretch matrix $\mathbf{V}$ can be expressed in terms of $\mathbf{F}$ by multiplying Eq. (2) with its transpose according to

$$\mathbf{F}\cdot\mathbf{F}^{\mathbf{T}} = \mathbf{V}\cdot\mathbf{R}\cdot\mathbf{R}^{\mathbf{T}}\cdot\mathbf{V}^{\mathbf{T}} = \mathbf{V}\cdot\mathbf{V} \tag{3}$$

where the relations $\mathbf{R}^{\mathbf{T}} = \mathbf{R}^{-1}$ and $\mathbf{V}^{\mathbf{T}} = \mathbf{V}$ are used. By solving the eigenproblem for $\mathbf{F}\cdot\mathbf{F}^{\mathbf{T}}$ the following relationships are easily obtained

$$\mathbf{F}\cdot\mathbf{F}^{\mathbf{T}} = \mathbf{V}\cdot\mathbf{V} = \lambda_1^2\mathbf{n_1}\mathbf{n_1^T} + \lambda_2^2\mathbf{n_2}\mathbf{n_2^T} + \lambda_3^2\mathbf{n_3}\mathbf{n_3^T} \Rightarrow \mathbf{V} = \lambda_1\mathbf{n_1}\mathbf{n_1^T} + \lambda_2\mathbf{n_2}\mathbf{n_2^T} + \lambda_3\mathbf{n_3}\mathbf{n_3^T} \tag{4}$$

where λ_i ($i = 1, 2, 3$) is an eigenvalue of $\mathbf{V}$ and $\mathbf{n_i}$ is the corresponding eigenvector. The true strain is then given by

$$\varepsilon = \ln\mathbf{V} = \ln\lambda_1\mathbf{n_1}\mathbf{n_1^T} + \ln\lambda_2\mathbf{n_2}\mathbf{n_2^T} + \ln\lambda_3\mathbf{n_3}\mathbf{n_3^T} \tag{5}$$

The deformation gradient matrix can be expressed in terms of the displacements u, v and w (x, y and z-direction). The expression is given by

$$\mathbf{F} = \begin{pmatrix} 1+\frac{\partial u}{\partial x} & \frac{\partial u}{\partial y} & \frac{\partial u}{\partial z} \\ \frac{\partial v}{\partial x} & 1+\frac{\partial v}{\partial y} & \frac{\partial v}{\partial z} \\ \frac{\partial w}{\partial x} & \frac{\partial w}{\partial y} & 1+\frac{\partial w}{\partial z} \end{pmatrix} \tag{6}$$

Only the in-plane components in the upper left 2×2 submatrix are detected by the experiment technique (DSP). But by assuming that the in-plane displacements u and v are constant through the thickness, i.e. $\frac{\partial u}{\partial z} = \frac{\partial v}{\partial z} = 0$, the incompressibility condition $\det\mathbf{F} = 1$ is simplified to

$$\left(1+\frac{\partial w}{\partial z}\right)\cdot\det\mathbf{F_{2D}} = 1, \quad \mathbf{F_{2D}} = \begin{pmatrix} 1+\frac{\partial u}{\partial x} & \frac{\partial u}{\partial y} \\ \frac{\partial v}{\partial x} & 1+\frac{\partial v}{\partial y} \end{pmatrix} \tag{7}$$

The in-plane components of the strain matrix are obtained by solving the eigenproblem according to Eq. (4) based on the two-dimensional description of the deformation gradient matrix $\mathbf{F_{2D}}$. The out-of-plane strain component ε_z is finally derived by from Eq. (7) as

$$\varepsilon_z = \ln\left(1+\frac{\partial w}{\partial z}\right) = \ln\left(\frac{1}{\det\mathbf{F_{2D}}}\right) \tag{8}$$

The deformation gradients in Eq. (7) contain derivatives, which are approximated by differentials. Since noise tends to get magnified by numerical differentiation, strains need to be calculated with some care. Therefore a first-order Savitsky–Golay filter (Press et al., 1992; Kajberg and Sjödahl, 2003) is applied to the displacement components u and v. This filter is basically a method to fit a plane to local data in a least-square sense. The local data chosen in this experiment consist of displacement data for 3×3 square grids. An example of such a square grid is shown in Fig. 4(a), where the nine data points are marked with circles. The displacement component v for these nine points is marked with circles in Fig. 4(b), where the fitted plane also is shown. The equations of the planes for each in-plane displacement component are

$$\begin{cases} u' = u + u_{,x}x + u_{,y}y \\ v' = v + v_{,x}x + v_{,y}y \end{cases} \tag{9}$$

where $u_{,x} = \frac{\partial u}{\partial x}$, etc. u, $u_{,x}$, $u_{,y}$ and v, $v_{,x}$, $v_{,y}$ are fitted data for the planes and these data are assigned to each of the midpoints of the 3×3 square grids. These quantities inserted into $\mathbf{F_{2D}}$ in Eq. (7) finally yields information necessary to evaluate the strain components, ε_x, ε_y, ε_z and the shear component ε_{xy}. Finally a slightly modified expression for the equivalent plastic strain is defined as

$$\varepsilon_{\mathrm{ep}} = \sqrt{\tfrac{2}{3}(\varepsilon_x^2 + \varepsilon_y^2 + \varepsilon_z^2 + 2\varepsilon_{xy}^2)} \tag{10}$$

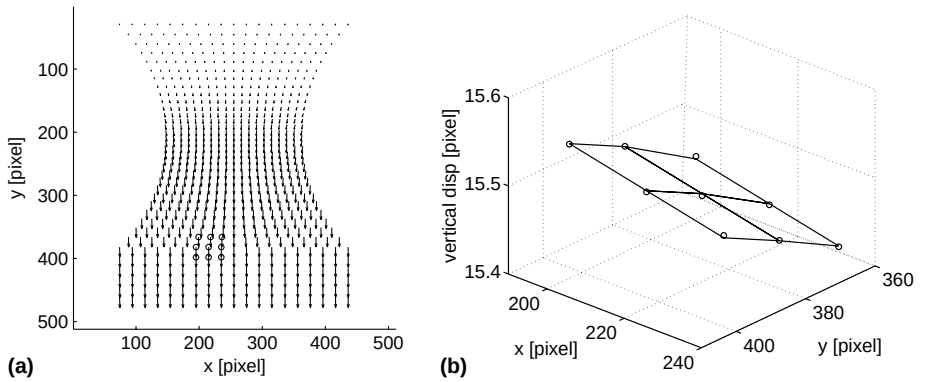

Fig. 4. Displacement field (a). Local displacement field (b).

Note, that the two unknown shear components are not considered. Later FE-analysis will show that this strain expression is a good approximation of the common expression for the plastic equivalent strain since the two excluded shear components are relatively small.

2.3. Uncertainties

As a measure of the reliability of the experimental results the uncertainties of the evaluated quantities are used. These uncertainties are influenced by the arising errors corresponding to the speckle displacement evaluation. Further, the regression model for the filtered displacement values in Eq. (9) affects the resulting uncertainties.

As mentioned in the previous subsection every displacement evaluation step contains small errors. These errors are dependent on the correlation values from the DSP-calculations and the size of the speckles and the subimages (Sjödahl, 1997). Since the displacement state at a certain instant is determined by adding incremental results from the DSP-evaluations the total error will be a consequence of errors corresponding to all incremental displacement steps used. If the displacement increment errors e_i are random and independent the square of the total error at a certain instant m can be expressed in terms of a cumulative sum of squared errors as

$$e_m = \sqrt{\sum_{i=1}^{m} e_i^2} \tag{11}$$

The relation between the total displacement error e_m and the uncertainties of the filtered values of displacements and strains are presented in detail in Appendix A. The resulting uncertainties are given by

$$s_u = s_v = 0.333 e_m$$

$$0.023 e_m \leqslant s_{\varepsilon_{\mathrm{ep}}} \leqslant 0.045 e_m \tag{12}$$

where s_u and s_v are uncertainties in evaluated displacements u and v, respectively. The strain uncertainty $s_{\varepsilon_{\mathrm{ep}}}$ depends on the position for field data evaluation. The lower value corresponds to regions, where the subimages are most separated and the higher value corresponds to the midpoint of the specimen.

3. Constitutive models

Two types of constitutive models, which both are based on isotropic hardening, are chosen in order to describe the strain hardening. The first model is a piecewise linear plasticity model based on five parameters, where the first one is the initial effective yield stress σ_0 and the other four define strain hardening moduli (slopes) $[H_1, H_2, H_3, H_4]$ initiated at different equivalent plastic strain levels. The levels depend on the material studied and are 0, 0.1, 0.25 and 0.6 for Domex 355 and 0, 0.075, 0.2 and 0.4 for Domex 650. The second model is a parabolic hardening description, in which the effective stress σ_e according to von Mises is given by

$$\sigma_e = A + B\varepsilon_{ep}^n \tag{13}$$

where A, B and n are three material parameters. Finally, the elastic properties are given by Young's modulus $E = 210$ GPa and Poisson's ratio $v = 0.3$.

4. Finite element modelling

The numerical modelling of the experiments is based on finite element analysis (FEA). Due to the low displacement rates inertia forces are neglected and the analysis is performed under static conditions. The chosen FE-code MSC.Marc (2003) uses an implicit time integration scheme to solve the equilibrium equations.

4.1. FE-mesh

Since the specimens are designed to achieve strain localisation symmetric along the horizontal (x-)axis and the vertical (y-)axis only one 8th of specimens are modelled. In other words, the localised neck is assumed to appear perpendicular to the loading direction and not inclined at an angle as in Fig. 1. The FE-mesh consists of 3-D eight node brick elements with eight integration points. There are two elements in the thickness direction and totally 512 elements are used in the entire mesh (see Fig. 5(a)). In order to model the symmetries with all three coordinate planes, necessary boundary conditions are used. The controlled displacement in the vertical direction, denoted v, is applied at the lower end of the modelled part of the specimens (see Fig. 5(a)).

4.2. Adaptive meshing

The simulations of the experiments contain large deformation resulting in highly distorted elements, which is associated to large errors. Therefore, some kind of remeshing has to be performed. There are a couple of so-called adaptive meshing techniques at hand (Huerta et al., 1999). The adaptive procedure is a tool for assessing the error of the solution and an algorithm to define a new FE-discretisation. Two different approaches may be used to assess the error: error estimators or error indicators. The error estimators approximate a measure of the actual error in a given norm. The norm can be based on the error criteria concerning strain energy, effective stress, plastic strain, etc. The other approach, namely error indicators, are chosen in a more ad hoc manner. Typical error indicators are for example that certain effective stress or plastic strain levels indicate that a mesh refinement has to be performed. Note that the indicators do not quantify the actual error, instead intuitive considerations control the mesh adaptivity. For all approaches it is of importance to decide how frequently the mesh refinement should be performed. For a

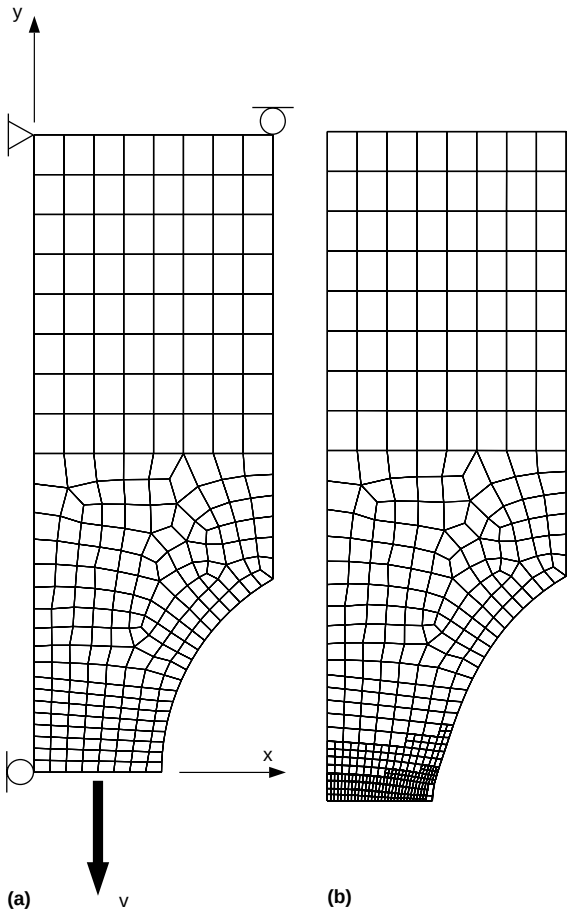

Fig. 5. FE-Mesh with applied boundary conditions and controlled vertical displacement (a). The mesh at the end of the simulation with the adaptive refinements performed (b).

3-D FE-simulation one refinement generates eight new elements for every element that does not satisfy the chosen error criterion. In practise the number of refinement steps has to be restricted in order to limit the number of elements and thereby achieving reasonable computation times. For example, the error criterion do not have to be checked for every increment, or only two or three refinement steps are allowed.

The computation time is of great importance for the suggested method for parameter estimation since the inverse modelling procedure implies a large number of simulations. Therefore the choice of adaptive method is a compromise between the accuracy in the FE-results and the duration of the simulations. Here, the error indicator approach is chosen and the number of refinement steps is limited to two. The indicator is based on the equivalent plastic strain and the elements are refined when their plastic strain reach any of two prescribed strain levels. The levels depend on which material is studied. For Domex 355 the levels are set to 0.25 and 0.5 strain. The corresponding levels for Domex 650 are 0.2 and 0.4 strain. The lower values for Domex 650 are chosen because fracture occurs earlier for that material than for Domex 355. The mesh for the last increment, when all refinement steps are performed, is shown in Fig. 5(b).

5. Inverse modelling

To describe the idea of inverse modelling the outline by Tarantola (1987) is appropriate: The scientific study of a physical system $\mathcal{M}$ (e.g. the elastic properties of an anisotropic material, see Fig. 6) can be divided into three steps. Firstly, a *parameterisation* of the system, which is a complete description of $\mathcal{M}$ using a minimal set $\mathcal{P}$ of *model parameters*. Secondly, so-called *forward modelling*, which is finding the physical laws that, with a given set of model parameters, predict measured quantities belonging to $\mathcal{M}$. And finally, *inverse modelling*, where measured quantities belonging to $\mathcal{M}$ are used for deducing the values of the model parameters.

In the context of this work inverse modelling is used to estimate a set of parameters in a mathematical model of a steel material, i.e. a constitutive model describing the material response to loading. In general, the parameter values for the material model are not known and have to be determined based on experimental data, υ. If the model behaviour depends on a set of parameters $x_k \in \mathcal{P}$, where $k = 1, \ldots, p$ and if an error measure is defined, formulated as a least-square objective function, $f(x_k)$, describing the discrepancies between the model approximation and the experimental data υ, then the parameter estimation can be stated as an optimisation problem (see e.g. Mahnken and Stein, 1997). Hence, the objective is to minimise the error between data produced by the mathematical model $y(x_k)$ and experimental data υ, according to

$$\min f(x_k) = \min \frac{1}{2} \sum_{i=1}^{M} (\upsilon_i - y_i(x_k))^2. \tag{14}$$

Now, real experimental data is mostly accessible at discrete intervals (e.g. time or load steps) and the model generated data must be transformed to the observation space of experimental data. Thus, the resulting least-square function is discrete, as indicated above with $i = 1, \ldots, M$ as the number of experimental points.

5.1. Objective function

A crucial point in inverse modelling is the choice of objective function. In this paper, the objective function is a least-square functional with residuals based on the difference between experimental and FE-

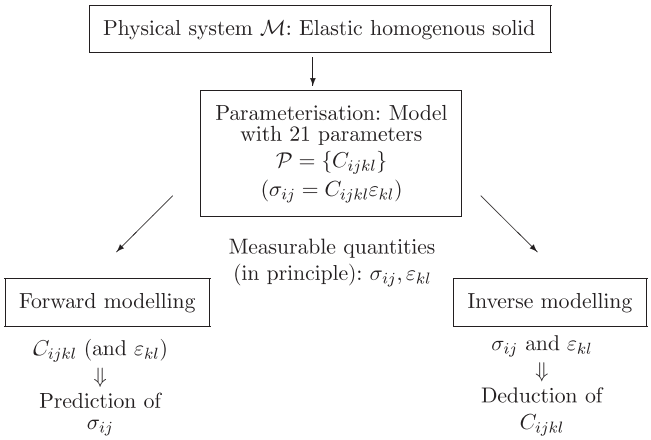

Fig. 6. Scientific study of a physical system (illustration) according to Tarantola (1987).

calculated data. The least-square criterion is justified based on the hypothesis that the sum of several different contributions will tend to be normally distributed, irrespective of the probability distribution of the individual contributions. This is often the case e.g. for measurement errors in the long run (Box et al., 1978).

The experimental data consists of four quantities measured and evaluated at time instants t_m. These are the in-plane displacements $u^{\exp}(t_m)$ and $v^{\exp}(t_m)$, the equivalent plastic strain $\varepsilon_{\mathrm{ep}}^{\exp}(t_m)$ and the loading force $F^{\exp}(t_m)$, which all are used when the objective function is formed. However, the measured quantities are of different physical dimensions and therefore some kind of normalisation has to be performed before summing all squares. Further, the influence of each quantity has to be tuned in order to get sum of squares of the same magnitude. Therefore, all residuals are normalised by basically scaling them with the difference between the maximum and mean value of the actual quantity. The sums of squares based on each individual quantity were studied and mutually compared after the parameter estimations had been performed. They were all of same magnitude. The objective function Φ is given by

$$\Phi_1 = \frac{1}{N-p}\sum_{m=1}^{M}\sum_{n=1}^{N_m}\left[\left(\frac{u_n^{\exp}(t_m)-u_n^{\mathrm{FE}}(t_m)}{|u^{\exp}(t_m)|_{\max}-|u^{\exp,\mathrm{mean}}(t_m)|}\right)^2+\left(\frac{v_n^{\exp}(t_m)-v_n^{\mathrm{FE}}(t_m)}{|v^{\exp}(t_m)|_{\max}-|v^{\exp,\mathrm{mean}}(t_m)|}\right)^2+\left(\frac{\varepsilon_{\mathrm{ep}}n^{\exp}(t_m)-\varepsilon_{\mathrm{ep}}n^{\mathrm{FE}}(t_m)}{|\varepsilon_{\mathrm{ep}}^{\exp}(t_m)|_{\max}-|\varepsilon_{\mathrm{ep}}^{\exp,\mathrm{mean}}(t_m)|}\right)^2\right],$$

$$N=\sum_{m=1}^{M}N_m$$

$$\Phi_2 = \frac{1}{M-p}\sum_{m=1}^{M}\left(\frac{F^{\exp}(t_m)-F^{\mathrm{FE}}(t_m)}{|F^{\exp}|_{\max}-|F^{\exp,\mathrm{mean}}|}\right)^2$$

$$\boxed{\Phi=\Phi_1+\Phi_2} \tag{15}$$

where p is the number of material parameters, N_m is the number of measure points at a certain time instant t_m and M is the number of instants. Typical values of N_m and M are 627–703 and 11–15, respectively.

5.2. Interpolation of numerical field information

The DSP-algorithm used in the experiments for displacement and strain evaluation results in pointwise field information with measure points according to the initial grid configuration shown in Fig. 3(a). However, the displacement and strain data in the FE-calculation are associated to the node coordinates. (MSC.Marc extrapolates the element strains from the integration points to the element nodes.) In order to compare numerical data with experimental data the FE-results are interpolated to points that coincide with the points in the initial grid configuration (experiment). The numerical values at the grid points are determined by linear interpolation between the values of the three closest nodes (FE-model). In other words, all grid points lie in triangular regions, where the nodes are the apex points. These triangular regions are determined by the so-called Delaunay triangulation (Edelsbrunner, 2001), which creates a unique mesh of triangles.

5.3. Optimisation method

Different algorithms can be used to solve the optimisation problem (14), or more specific in this work, minimisation of the function in Eq. (15). In general it is possible to categorise the algorithms in zero-order methods, where only objective function evaluations are necessary (e.g. Simplex and Monte Carlo methods) and first-order methods, with additional need for gradient evaluation of the least-square objective function (e.g. Gauss–Newton and Levenberg–Marquardt).

The optimisation procedures in this work are performed with INVSYS (Wikman and Bergman, 2000), an in-house programming system designed for analysis of inverse problems. A finite element analysis is used as the direct problem and the input data (e.g. material parameters) are varied in an attempt to reach desired output data from the analysis and thereby minimise the objective function value. The core of the system is an optimisation algorithm, the unconstrained subspace-searching simplex method (SUBPLEX) (Rowan, 1990). The method uses direct search to find the minimum of the objective function, meaning that no numerical or analytical estimate of the function derivative is necessary. Instead only the function value is sequentially evaluated and compared to find optima (i.e. a zero-order method).

SUBPLEX is a generalisation of the Nelder–Mead simplex method (NMS) (Nelder and Mead, 1965) which is an optimisation algorithm capable of minimising very noisy objective functions. However, NMS is not computationally effective when the number of parameters is large. SUBPLEX therefore divides the p-dimensional parameter space into subspaces of maximum five parameters and uses NMS with periodic restarts to reach the optimum value for the objective function.

It is often necessary to infer some type of constraints to solve the optimisation problem. Two types of constraints can be handled by INVSYS. Firstly, side constraints that are direct limitations on the model parameters (e.g. lower and upper bounds) or some fixed relative value of a group of parameters. Secondly, behaviour constraints on some solution variable in the direct problem (e.g. maximum stress or displacement values in the direct problem FEA). Both types of constraints are handled by converting the constrained problem to a sequence of unconstrained problems. This is done by adding a penalty function to the objective function (Moe, 1973).

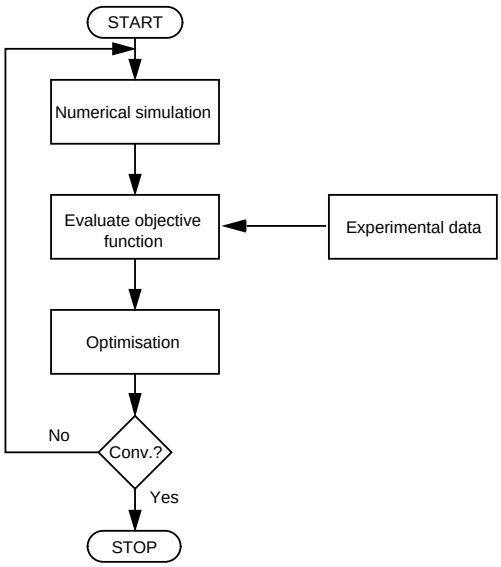

Fig. 7. Flow scheme for an inverse problem.

Only the first type of constraints is used in the two chosen constitutive models. The piecewise linear plasticity model is constrained to result in a monotonously decreasing slope of the stress–strain curve. Hence, the strain hardening moduli follow $H_1 \geqslant H_2 \geqslant H_3 \geqslant H_4 \geqslant 0$. Further, the initial yield stress σ_0 is given a lower and upper bound. The bounds are 300 and 450 MPa, and 600 and 750 MPa for Domex 355 and Domex 650, respectively. The second constitutive model, the parabolic hardening description, is given the following constraints.

Material	Domex 355			Domex 650		
Parameters	A [MPa]	B [MPa]	n	A [MPa]	B [MPa]	n
Lower bound	300	200	0.4	600	300	0.4
Upper bound	450	600	0.7	750	700	0.7

5.4. Parameter estimation

The iterative estimation procedure; FEA, objective function calculation and parameter optimisation is controlled by user supplied interface programs, managing communication and interface between the utilised program applications. Output from INVSYS after each iteration defines a new set of model parameters used for successive analysis of the direct problem. When a global minimum is found for the objective function, the resulting parameters are considered as a best-fit for the model in question. The inverse analysis is terminated either when a maximum number of (objective) function evaluations is reached or when the change in parameter values during two subsequent function evaluations are less than a specified tolerance (in this case 10^{-3}). The scheme from start to stop of an inverse problem is described in Fig. 7.

6. Results and discussion

The estimated parameters and the objective function values based on the two chosen constitutive models are presented in Tables 1 and 2 for Domex 355 and Domex 650, respectively. As expected, the objective function values Φ_{PWL} corresponding to the piecewise linear plasticity model with five parameters achieved somewhat lower values than the objective function Φ_{PH} corresponding to parabolic hardening model with its three parameters. The results of the estimations are visualised as stress–strain curves in Figs. 8 and 9. Further, stress–strain curves based on average values of the estimated parameters (last row in Tables 1 and 2) are depicted in Fig. 10. Note that the stress–strain relationships determined by the standardised tension tests also are included in these figures. The curves corresponding to the two chosen constitutive models show a good agreement with the standardised stress–strain curves. Further, the curves based on the

Table 1
Material parameters and objective function values for Domex 355

Spec. no.	Φ_{PWL} [10^{-1}]	σ_0 [MPa]	H_1 [MPa]	H_2 [MPa]	H_3 [MPa]	H_4 [MPa]	Φ_{PH} [10^{-1}]	A [MPa]	B [MPa]	n [10^{-1}]
1	4.63	395	1190	541	289	103	5.91	356	434	4.56
2	2.69	386	1400	592	123	107	4.82	355	447	4.15
3	2.76	398	1320	518	269	0.01	3.97	368	432	4.49
4	3.30	422	1310	414	248	0.10	5.04	432	387	5.44
5	7.48	403	1270	459	297	0.04	9.30	379	403	4.36
Av. val.		401	1300	505	245	42		378	421	4.60

Table 2
Material parameters and objective function values for Domex 650

Spec. no.	Φ_{PWL} [10^{-1}]	σ_0 [MPa]	H_1 [MPa]	H_2 [MPa]	H_3 [MPa]	H_4 [MPa]	Φ_{PH} [10^{-1}]	A [MPa]	B [MPa]	n [10^{-1}]
1	4.04	672	1640	546	338	1.62	6.08	717	436	6.79
2	3.96	666	2060	689	411	0.74	5.52	655	517	4.44
3	5.77	655	2070	785	366	0.09	9.21	651	554	5.27
4	4.96	671	1670	522	412	0.08	7.07	706	441	6.42
5	3.66	651	2090	738	217	0.13	6.22	678	491	5.35
Av. val.		664	1910	656	349	0.53		682	488	5.65

piecewise linear plasticity model have almost no strain hardening at high strain levels. An inspection in Fig. 10 shows that the more simple parabolic hardening model with less parameters could not cover this lack of strain hardening.

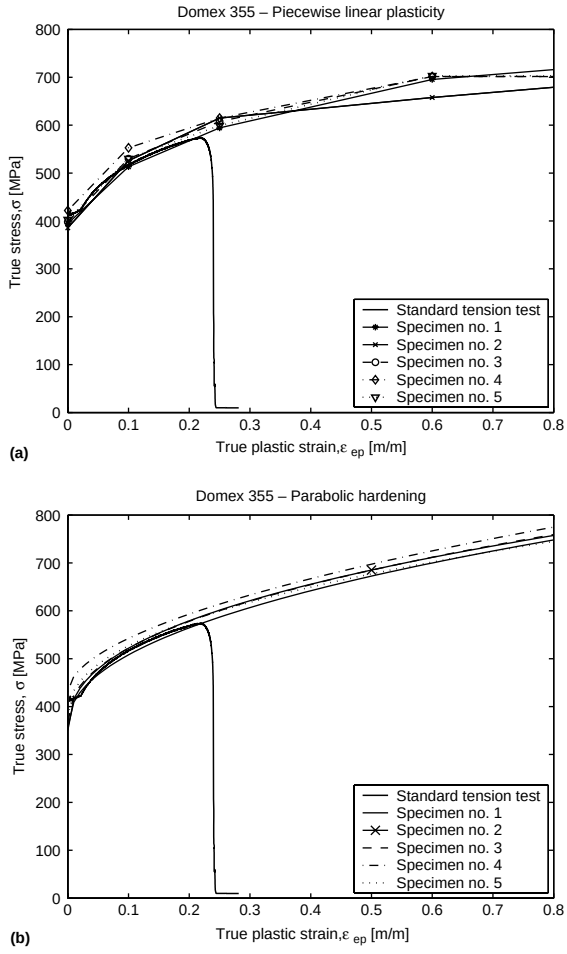

Fig. 8. Stress–strain curves for Domex 355. Curves for the piecewise linear plasticity model (a). Curves for the parabolic hardening model (b).

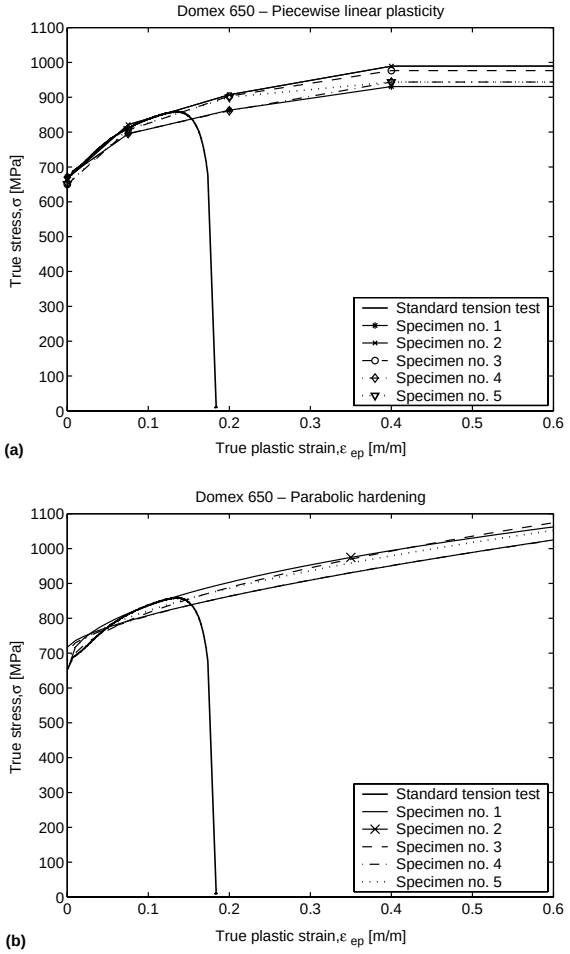

Fig. 9. Stress–strain curves for Domex 650. Curves for the piecewise linear plasticity model (a). Curves for the parabolic hardening model (b).

The equivalent plastic strain presented in Figs. 8–10 are limited by the maximum measured strain, namely the strain at fracture. These strain values are presented in the table below, where Domex 355 appears to be the more ductile material.

Material	Domex 355					Domex 650				
Spec no.	1	2	3	4	5	1	2	3	4	5
$\varepsilon_{ep}^{fracture}$	0.76	0.76	0.70	0.75	0.78	0.55	0.60	0.55	0.55	0.60

The time to accomplish a parameter estimation depends on the time to complete a FE-simulation and the number of iterative steps in the optimisation procedure. More iterative steps were necessary for convergence of the parameters corresponding to the piecewise linear plasticity model. The computation time was about 150 s and 356–808 steps and 118–191 steps were needed for the piecewise linear plasticity model and the parabolic hardening model, respectively. Thus, the average time to accomplish a parameter

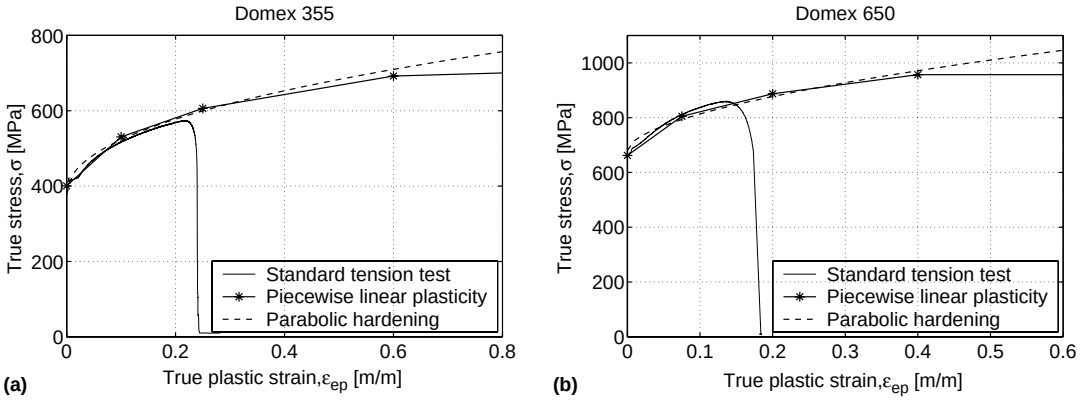

Fig. 10. Stress–strain curves for each constitutive model based on mean values of the estimated parameters. Stress–strain curves for Domex 355 (a). Stress–strain curves for Domex 650 (b).

estimation was approximately 6 and 23 h, respectively. The FE-simulations was performed on a PC with a 1.9 GHz processor.

As mentioned in Section 2.2 a modified equivalent plastic strain was defined according to Eq. (10). It was implemented in MSC.Marc and the FE-analyses showed only a small discrepancy between this strain measure and the common equivalent plastic strain with all shear components included. The largest relative discrepancy of 1% appears in the necking region for the last instant. For earlier times no significant difference is obtained. The modified strain measure is concluded as a good approximation of the common measure for equivalent plastic strain.

The uncertainty analysis resulted in displacement uncertainties increasing with respect to the evaluation step as a square root function from approximately 0.47 to 1.7 μm. The same behaviour is obtained for the equivalent plastic strain with uncertainties in the interval from approximately 0.0015 to 0.0056.

In order to illustrate the coincidence between the experimentally determined quantities and FE-calculated quantities, the strain fields for some instants are presented in Fig. 11. The fields correspond to specimen no. 1 of the Domex 355 steel, where the FE-calculated fields are based on the piecewise linear plasticity model. The experimentally determined strain fields are placed to the left, while the FE-calculated fields are shown to the right. By comparing the fields corresponding to the different occasions the same general appearance during the deformation process can be seen.

The presented parameter estimation is based on the objective function according to Eq. (15), where all measured quantities are used. Other functions were also tested. For example, an objective function without the force response, i.e. $\Phi = \Phi_1$, was tried. The subsequent optimisation resulted in parameters that gave very incorrect stress–strain curves, where the initial strain hardening was very high. Thus, the FE-calculated plastic strain never reached the levels beyond the strain when necking occurs in standard tension tests. A comparison between the measured force $F^{\exp}$ and the calculated reaction force F^{FE} also showed that F^{FE} achieved much higher values. However, constitutive modelling without any force correlation is questionable and the discussion above demonstrates the weaknesses.

A more interesting objective function considering statistical foundations is the so-called chi-square formulation, denoted χ^2. Typical for χ^2 is that the residuals, i.e. difference between experimental data and numerical data, are weighted with the variances corresponding to the experimental data. Thereby, more accurate experimental data is given higher importance. An example of a χ^2-function, based on the quantities and parameters defined in Eq. (14), is given by

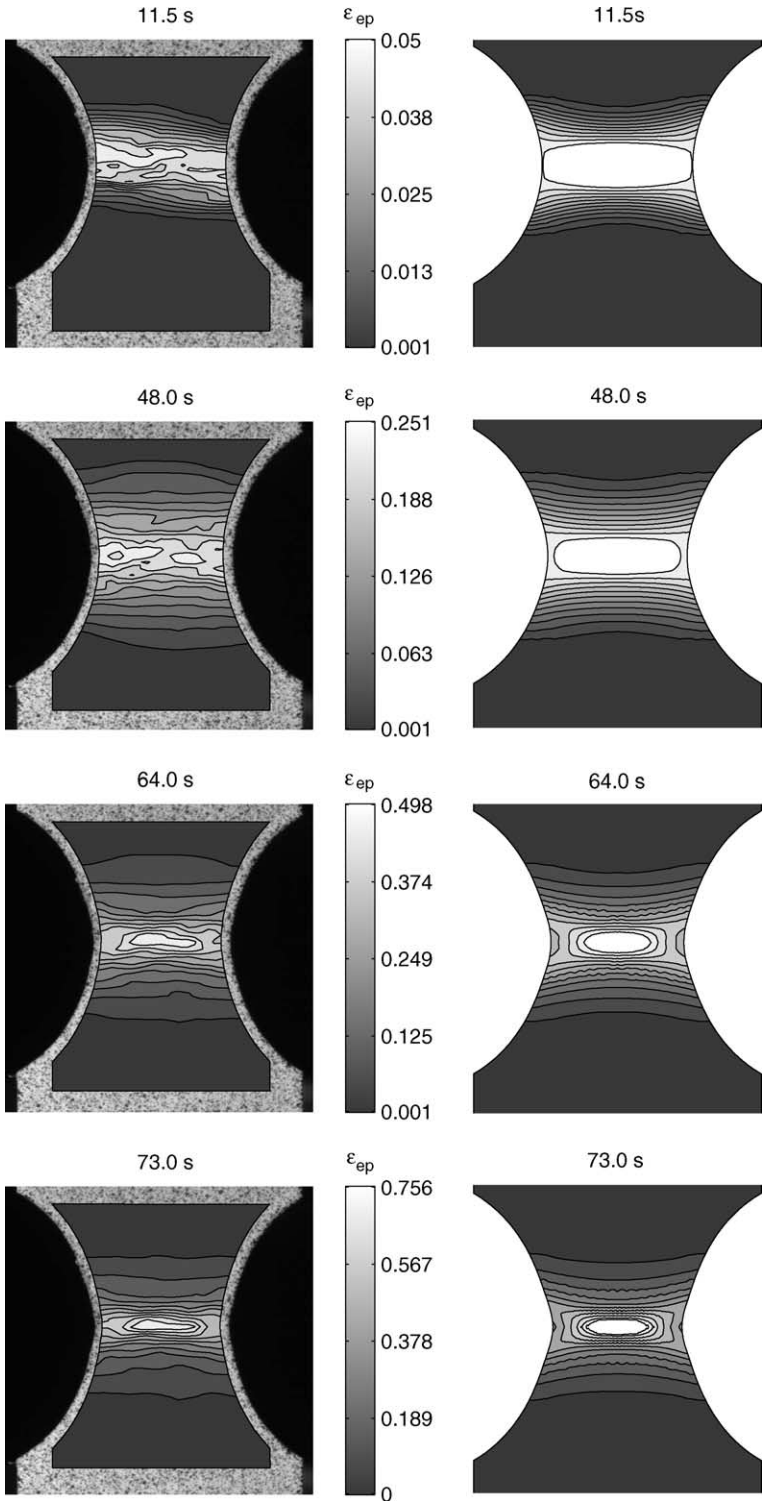

Fig. 11. Strain fields for specimen no. 1 (Domex 355). The experimentally determined fields are placed to the left. The FE-calculated ones are placed to the right. Note the different strain scales.

$$\chi^2 = \frac{1}{M-p}\sum_{i=1}^{M}\frac{[v_i - y_i(x_k)]^2}{s_v^2 i}$$

where $s_v^2 i$ is the variance of v_i. Further, the χ^2-function provides a statistical measure of goodness-of-fit. As long as the squared residuals $[v_i - y_i(x_k)]^2$ have values below their variances $s_v^2 i$ the chosen model with corresponding parameters describes the physical system well. A rule of thumb is that a "typical" value of χ^2 for a "moderately" good fit is approximately equal to one. The DSP-algorithm provides the variances for the displacement and strain data. The variances are namely the square of the uncertainties estimated in Appendix A (Uncertainty analysis) and presented above. However, the χ^2-formulation is not implemented in this paper because the numerical data, i.e. the FE-calculated quantities, are subjected to discretisation errors, which are difficult to estimate. It is assumed that these errors are larger than the experimental errors and the χ^2-formulation is therefore rejected for the present.

7. Conclusions

A method for characterisation of materials subjected to large strains is presented. Material parameters in two types of constitutive models are estimated by inverse modelling, where a least-square functional is minimised. The least-square functional, denoted objective function, is based on the difference between experimentally and numerically determined field information provided by the DSP-technique and FEA, respectively.

The implemented adaptive meshing conditions in MSC.Marc worked well and a good compromise between a short computation time and a FE-mesh with not highly distorted elements was fulfilled.

The choice of objective function gave a good balance between the influence of the measured quantities. However, the rejected χ^2-formulation discussed in the previous section has advantages, e.g. the goodness-of-fit measure, that attracts to further investigation and evaluation.

With the presented methodology for field measurement the development of strain is tracked from initial plasticity to fracture. Since it is possible to detect the strain state at fracture the full-field measurement might be of interest in for example damage mechanics. Furthermore, when obtaining so-called forming limit diagrams (FLD) by biaxial tension testing the DSP-method might be useful in the determination of essential quantities, namely the principal strains. A common technique for detecting strains for FLD is by etching a regular texture on the surface of the specimen. However, the speckle method has the advantage that it does not effect the material, which is the case when etching is performed.

The presented method is here used for an isotropic material but it also seems likely that characterisation of anisotropic materials would function well.

Acknowledgements

The authors are grateful to Dr. K.-G. Sundin, Dr. Bengt Wikman and Dr. Hans-Åke Häggblad for their contributions and comments on the manuscript. The financial supports from Complab, *Centre for testing and development of mechanical components*, and the Polhem Laboratory, *Competence center for integrated product development*, are gratefully acknowledged.

Appendix A. Uncertainty analysis

In order to estimate the uncertainties of the quantities u, v and ε_{ep}, the regression model for fitting displacement data to planes has to be studied. The regression model for the second equation in Eq. (9) is

shown in Eq. (A.1) below. A similar model is used for the first equation in Eq. (9). However for simplicity the following analysis is made for the vertical displacement component, v.

$$\boldsymbol{v}' = \boldsymbol{X}\boldsymbol{\beta} + \boldsymbol{\epsilon} \tag{A.1}$$

$\boldsymbol{v}'$ is a 9×1 vector of expected values for the displacement component v in the nine points of one of the 3×3 grids. $\boldsymbol{X}$ is the 9×3 matrix of the so-called independent variables given by

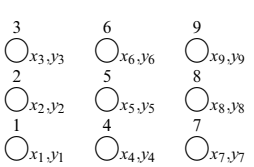

$$\boldsymbol{X} = \begin{pmatrix} 1 & \Delta x_1 & \Delta y_1 \\ 1 & \Delta x_2 & \Delta y_2 \\ 1 & \Delta x_3 & \Delta y_3 \\ 1 & \Delta x_4 & \Delta y_4 \\ 1 & 0 & 0 \\ 1 & \Delta x_6 & \Delta y_6 \\ 1 & \Delta x_7 & \Delta y_7 \\ 1 & \Delta x_8 & \Delta y_8 \\ 1 & \Delta x_9 & \Delta y_9 \end{pmatrix} \tag{A.2}$$

where column 2 and 3 consist of the pixel coordinates relative the midpoint (x_5, y_5), i.e. $\Delta x_i = x_i - x_5$ and $\Delta y_i = y_i - y_5$, where $i = 1, \ldots, 9$. Further, the 3×1 vector, $\boldsymbol{\beta}$, is a vector with the quantities $(v, v_{,x}, v_{,y})$ for the fitted plane. Finally the 9×1 vector $\boldsymbol{\epsilon}$ contains independent normal distributed experimental errors. The quantities v, $v_{,x}$ and $v_{,y}$ are determined by taking the least-square estimate, b, of $\boldsymbol{\beta}$ (Box et al., 1978) as shown in Eq. (A.3).

$$\boldsymbol{b} = \begin{pmatrix} v \\ v_{,x} \\ v_{,y} \end{pmatrix} = [\boldsymbol{X}^{\mathrm{T}}\boldsymbol{X}]^{-1}\boldsymbol{X}^{\mathrm{T}}\boldsymbol{v}' \tag{A.3}$$

One way to estimate the uncertainties is by setting them equal to the corresponding standard deviations of the quantities, $v, v_{,x}$ and $v_{,y}$. Therefore, the variances of the parameters are calculated. The variance-covariance matrix used in least-squares calculation is given by (Box et al., 1978)

$$V(\boldsymbol{b}) = [\boldsymbol{X}^{\mathrm{T}}\boldsymbol{X}]^{-1}e_m^2 \tag{A.4}$$

where e_m is the displacement error at a certain instant m. Finally the standard deviations of the quantities are calculated by taking the square root of the diagonal elements of $V(\boldsymbol{b})$.

$$S(\boldsymbol{b}) = \sqrt{\mathrm{diag}(V(\boldsymbol{b}))} = \sqrt{\mathrm{diag}([\boldsymbol{X}^{\mathrm{T}}\boldsymbol{X}]^{-1})}e_m \Longleftrightarrow \begin{pmatrix} s_v \\ s_{v_{,x}} \\ s_{v_{,y}} \end{pmatrix} = \begin{pmatrix} S_1 \\ S_2 \\ S_3 \end{pmatrix} e \tag{A.5}$$

This uncertainty analysis is also performed for the displacement in the x-direction. That gives the same values for the standard deviations as in Eq. (A.5). However, the standard deviations $s_{u_{,x}}$ and $s_{v_{,y}}$ are related to the engineering strains $u_{,x}$ and $v_{,y}$. For simplicity these standard deviations are also assumed for the true strains ε_x and ε_y. In order to estimate the uncertainty for the strain value of interest $\varepsilon_{\mathrm{ep}}$ the mean value of the strain uncertainties above are used. Hence the uncertainties of u, v and $\varepsilon_{\mathrm{ep}}$ are

$$\begin{pmatrix} s_u = s_v \\ s_{\varepsilon_{\mathrm{ep}}} \end{pmatrix} = \begin{pmatrix} S_1 \\ \frac{S_2+S_3}{2} \end{pmatrix} e \tag{A.6}$$

For an approximately Gaussian-shaped correlation peak the displacement error e_m (Sjödahl, 1997) is related to the radius of the peak σ by

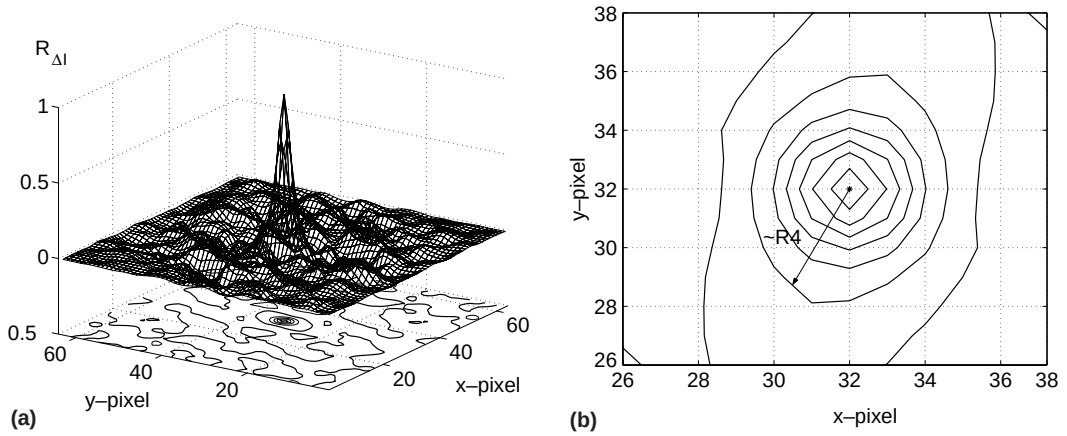

Fig. 12. Auto correlation surface (a). Level curves around the auto correlation peak (b).

$$e_m = 0.7\frac{\sigma^2}{B}\sqrt{\frac{1-c}{c}} \tag{A.7}$$

where σ is the radius of the correlation peak, B is the size of the subimage and c is the correlation values. The radius σ is possible to estimate without deforming any specimen. A subimage is chosen arbitrarily for every frame and by taking the auto correlation of the deviation of the intensity I the radius of the auto correlation peak gives the σ-value. The deviation is determined by $\Delta I = I - \langle I \rangle$, where $\langle I \rangle$ is the mean intensity. A typical auto correlation surface $R_{\Delta I}$ and its correlation peak are shown in Fig. 12. Further, the level curves for a region around the auto correlation peak is presented in Fig. 12(b), where also the radius is marked. All frames from all experiments gave approximately the same value of the radius, namely four pixels.

References

Adams, V., Askenazi, A., 1999. Building Better Products with Finite Element Analysis. On-Word Press, Santa Fe, USA. ISBN: 1-56690-160X.

ASTM Standard E8M-96, 1996. Standard test methods for tension testing of metallic materials [metric]. In: Annual Book of ASTM Standards, vol. 03.01, pp. 76–96.

Belytschko, T., Mish, K., 2001. Computability in non-linear solid mechanics. Int. J. Numer. Meth. Eng. 52, 3–21.

Bonet, J., Wood, R.D., 1997. Nonlinear continuum mechanics for finite element analysis. Cambridge University Press.

Box, G.E.P., Hunter, W.G., Hunter, J.S., 1978. Statistics for Experimenters. John Wiley & Sons.

Bridgman, P.W., 1952. Studies in Large Plastic Flow and Fracture. McGraw Hill, New York.

Edelsbrunner, H., 2001. Geometry and Topology for Mesh Generation. Cambridge University Press.

Faurholdt, T.G., 2000. Inverse modelling of constitutive parameters for elastoplastic problems. J. Strain Anal. 35 (6), 471–478.

Ghouati, O., Gelin, J.-C., 1998. Identification of material parameters directly from metal forming processes. J. Mater. Process. Technol. 80–81, 560–564.

Ghouati, O., Gelin, J.-C., 2001. A finite element-based identification method for complex metallic material behaviors. Comput. Mater. Sci. 21, 57–68.

Huerta, A., Rodriguez-Ferran, A., Diez, P., Sarrate, J., 1999. Adaptive finite element strategies based on error assessment. Int. J. Numer. Meth. Eng. 46, 1803–1818.

Kajberg, J., Sjödahl, M., 2003. Optical method to study material behaviour at high strain rates. In: Ståhle, P., Sundin, K.G. (Eds.), Proceedings of the IUTAM Symposium on Field Analysis for Determination of Material Parameters—Experimental and Numerical Aspects, Abisko National Park, Kiruna, Sweden, July 31–August 4, 2000. Kluwer Academic Publishers, Dordecht, the Netherlands, pp. 37–49.

Kajberg, J., Sundin, K.G., Melin, L.G., Ståhle, P., 2004. High strain-rate tensile testing and viscoplastic parameter identification using microscopic high-speed photography. Int. J. Plast. 20, 561–575.

Ling, Y., 1996. Uniaxial true stress–strain after necking. AMP J. Technol. 5, 37–48.

Mahnken, R., Stein, E., 1994. The identification of parameters for visco-plastic models via finite-element methods and gradient methods. Model. Simul. Mater. Sci. Eng. 2, 616–697.

Mahnken, R., Stein, E., 1997. Concepts and computational methods for parameter identification of inelastic material models. In: Owen, D.R.J., Õnate, P., Hinton, E. (Eds.), Computational Plasticity, Proceedings for COMPLAS 5, Barcelona, 17–20 March, 1997.

Moe, J., 1973. Penalty-function methods. In: Gallagher, R.H., Zienkiewicz, O.C. (Eds.), Optimum Structural Design, Theory and Applications.

Mori, K.-I., Yang, G., Osakada, K., 1995. Determination of optimal motion of tools in metal forming processes by controlled FEM simulation. Int. J. Machine Tools Manuf. 35 (6), 851–859.

MSC.Marc User's guide, version, 2003. MSC.Software Corporation, Santa ANA CA, USA.

Nelder, J.A., Mead, R., 1965. A simplex method for functional minimization. Comput. J. 7, 308–313.

Press, W.H., Teukolsky, S.A., Vetterling, W.T., Flannery, B.P., 1992. Numerical recipies in C, second ed. Cambridge University Press.

Rowan, T.H., 1990. Functional stability analysis of numerical algorithms. Ph.D. Thesis, The University of Texas at Austin, USA.

Sjödahl, M., 1994. Electronic speckle photography: increased accuracy by non-integral pixel shifting. Appl. Opt. 33, 6667–6673.

Sjödahl, M., 1997. Accuracy in electronic speckle photography. Appl. Opt. 36, 2875–2885.

Tarantola, A., 1987. Inverse Problem Theory, Methods for Data Fitting and Model Parameter Estimation. Elsevier Publisher B.V., New York, USA.

Wikman, B., Bergman, G., 2000. An inverse modelling system, user manual version 1.0. Technical report 2000:27, Luleå University of Technology, Luleå, Sweden.

Zhang, Z.L., Hauge, M., Øegård, J., Thaulow, C., 1999. Determining material true stress–strain curve from tensile specimens with rectangular cross-section. Int. J. Solids Struct. 36, 3497–3516.

Zhang, Z.L., Ødegård, J., Søvik, O.P., Thaulow, C., 2001. A study on determining true stress–strain curve for anisotropic materials with rectangular tensile bars. Int. J. Solids Struct. 38, 4489–4505.